Euro. Jnl of Applied Mathematics (2020), *vol.* 31, *pp.* 1002–1028 © The Authors 2019. Published by Cambridge University Press.
doi:10.1017/S0956792519000378

When a small thin two-dimensional body enters a viscous wall layer

R. A. PALMER and F. T. SMITH

Department of Mathematics, University College London, London WC1E 6BT, UK
emails: ryan.palmer.14@ucl.ac.uk; f.smith@ucl.ac.uk

(*Received 19 March 2019*; *revised 18 September 2019*; *accepted 22 November 2019*; *first published online 16 December 2019*)

If a body enters a viscous-inviscid fluid layer near a wall, then significant effects can be felt from the presence of incident vorticity, viscous forces and nonlinear forces. The focus here is on the response in the outer edge of such a wall layer. Nonlinear two-dimensional unsteady behaviour is examined through modelling, computation and analysis applied for a thin body travelling streamwise upstream or downstream or staying still relative to the wall. The wall layer with its balance between inviscid and viscous effects interacts freely with the body movement, causing relatively high magnitudes of pressure on top of the body and nonlinear responses in the gap between the body and the wall. The study finds explicit solutions for the motion of the body, separation of the flow arising near the wall and possible instabilities occurring over the length scale of any short body.

Key words: Viscous–inviscid interaction, fluid–solid interactions, boundary-layer theory

2010 Mathematics Subject Classification: Primary: 76D09; 74F10. Secondary: 76D10.

1 Introduction

Our interest lies in the effects of a small body entering a thin viscous wall layer of fluid flow at high flow rate. This is motivated by industrial applications, notably concerning the entry of a comparatively small ice crystal, shard of ice or other small body into the boundary layer on an aircraft or into an engine intake. Nonlinear effects in the fluid–body interaction are studied in the present work, with the motion of the body and that of the surrounding fluid flow influencing each other comparably.

The configuration of interest is near a fixed solid wall. The motivations for the work concern not only aircraft safety, for ice lumps, shards or other bodies such as debris or dust in a boundary layer of air flow on a wing [7, 19, 22], but also the transport of debris and dust in wider applications, and the movement of drugs or thrombi in blood vessel networks or lung airways, for example. Atmospheric flows are also of relevance here. Studies of fluid and body motions affecting each other substantially in near-wall shear flow with a single body or many bodies present are by [3, 4, 8, 15, 21, 35] for a boundary layer and by [12, 17, 26, 27] for channel flow. Laminar flow theory is addressed in [26, 27] whereas the works in [8, 4, 12, 15, 21] are mostly numerical or experimental on flow transition and those in [3, 17, 35] are concerned with computations or experiments on turbulent fluid motion. There is considerable interest in the generation of instabilities by such interactions, in related effects such as from feathers and other near-wall devices, and in discovering whether a body is attracted to or repelled from a nearby wall in general when

https://doi.org/10.1017/S0956792519000378 Published online by Cambridge University Press

nonlinear effects are significant: see [5, 6, 9, 13, 16, 36]. Here, [5] and [16] in particular address the influence of the Reynolds number and other parameters on attraction and repulsion, finding that either phenomenon can occur as the flow rate increases.

We mentioned several applications above. In terms of the ice crystal entering a boundary layer, sizes and distributions of particles whether crystals, bodies or debris vary considerably but typical values can be taken as follows. A cloud of ice crystals may have an ice crystal content (ICC) of the order of 10^{-3} to 10^{-2} kgm^{-3} and the volume ratio (assuming a density of order 1000 kgm^{-3}) gives a volume fraction between 10^{-6} and 10^{-5}. The size of particles is of the order 10^{-3} to 10^{-5} m, while the spacing between particles is approximately between 40 particle diameters (for ICC 10^{-2} kgm^{-3}) and 80 particle diameters (for ICC 10^{-3} kgm^{-3}). So 2×10^{-6} m particles have an average spacing of 0.8×10^{-3} m or 1.6×10^{-3} m (assuming a cubic configuration). Typically, the particle Reynolds number here is 10^2 to 10^3 and the global Reynolds number may be 10^4 to 10^6. For further details on icing conditions and the range of physical parameters, see the discussion in [14]. Some caution is necessary however on the theoretical front regarding an aim to make firm practical predictions. At the current stage, since the applied-mathematical theory of dynamic fluid–body interaction is still rather in its infancy, further explorations are required to discover which scenarios are amenable to rational study. (The present exploration leads on to comparisons with the ice-crystal application which are discussed at the end of the paper.)

We note a long-term need to address in a rational way the possible impacts and clashes between a moving body and a wall, cf [26, 27, 33], and to understand more about separations and eddy formations in the nearby flows either on the body or on the wall. These aspects also require inclusion of nonlinear effects. Again, understanding of scales and parametric effects governing the interactive behaviour is important. The recent findings of [33] and [24] suggest certain features in the linear regime as follows. These focus on the effects on body lift and moment from different lengths and locations of a body, thickness ratios and time scales, and, broadly, those effects act to destabilise the surrounding fluid motion, although several stabilising features are found, most notably from sufficient flexibility of the wall or the body or from slight streamwise movements of the body. The prime parameters highlighted in these two papers include the density ratio between the body and the fluid, the characteristic Reynolds number, the fluctuation amplitude and the relative dimensions of the body compared with the typical flow thickness of the boundary layer or channel.

The above comments on flow separations, stability and instability raise interest in the nonlinear effects of a body moving upstream or downstream relative to a nearby fixed wall. The body of concern in the present work is a thin body, subjected to both viscous influences and nonlinear inertial influences from the surrounding fluid flow. We have found no previous work on a small finite body in a viscous-inviscid wall layer. The present paper deals with fluid–body coupling in a boundary layer or channel flow for a relatively short body moving freely inside a viscous wall layer such that the thicknesses of the body and the wall layer are comparable. The interactions are considered for two spatial dimensions. The effective Stokes number of these interactions is assumed to be of order unity in the sense that overall the body neither follows the fluid streamlines closely as for a perfect tracer nor continues along its initial trajectory with ballistic behaviour, in general. The typical Reynolds number is large however and so the near-wall behaviour is very sensitive within the viscous wall layer. The representative Froude number is large and hence gravity is nominally negligible. The interplay of body movement and fluid

https://doi.org/10.1017/S0956792519000378 Published online by Cambridge University Press

dynamics here thus has significant inertial and viscous components present along with fully nonlinear effects, which can provoke flow separations. The unsteadiness is another substantial component in the sense of the combined evolution of the fluid flow and the body position with time starting from an initial-value state.

The major spatial scales involved are those of the viscous wall layer, but supplemented by those of a smaller adjustment zone which surrounds the leading edge of the thin body and adjusts the behaviour there in response to conditions downstream, while the major temporal scale is that of the body movement. Here, the basic setting has fluid–body interaction in the presence of an incident uniform shear flow close to a fixed wall.

Section 2 describes the coupling that is induced for the laminar two-dimensional (2D) flow involving unsteady interactions with the body movement. In the wall layer, a so-called condensed flow, where interaction with the flow outside the viscous wall layer is negligible, is induced which is governed by the nonlinear boundary-layer equations. The main interactions are derived for the boundary layer on an airfoil, to be specific. The same problem holds for channel flow however and for atmospheric boundary layers, for example. Section 3 addresses the behaviour when the body is initially sited in the outer reaches of the wall layer, a case which admits much analytical progress as well as being of practical concern. Sections 4 and 5 consider the resulting responses in steady flow and unsteady flow, respectively. Attention is given to the effects of a small velocity u_c of the body being positive, zero or negative relative to the wall, and the unknown scaled wall pressure, body pressures and scaled wall shear stress are of interest throughout. Section 6 presents further discussion and conclusions together with an assessment of the relevance to practical applications. (An Appendix A describes the background scales and an Appendix B shows the influence of flexibility in the body shape.)

2 The fluid–body coupling

The working below, for the flow around a comparatively thin short body that is moving freely near the wall, is expressed in terms of non-dimensional flow velocities (u, v), corresponding Cartesian coordinates (x, y), time t and pressure p. The dimensional versions are $U^*(u, v)$, $L^*(x, y)$, L^*t/U^* and $\rho^*U^{*2}p$, respectively. In the boundary-layer scenario, as shown in the sketch in Figure 1, fluid is flowing along an effectively flat surface, or wall, and far from the wall the free stream is moving with a given constant velocity parallel to that wall. The figure gives the relatively close-up view of a small thin body within the boundary layer near an airfoil surface, for example. Our aim is to describe the fluid flow around the body as well as the body movement itself with the change in the fluid flow due to the presence of the body being largely a local nonlinear change. Here, U^* is the representative fluid velocity, taken to be the free-stream value, while L^* is the airfoil chord, ρ^* is the uniform density of the incompressible fluid and the temporal factor L^*/U^* taken is the typical transport time. The velocity vector (u, v), pressure p and coordinates x, y are generally of order unity except near the wall which is located along the axis $y = 0$. In particular, (u, v) is given by $(1, 0)$ in the far field and the leading edge of the airfoil is taken as the origin. The Reynolds number is given by $Re = U^*L^*/\nu^*$, where ν^* is the uniform kinematic viscosity of the fluid. The representative length of the body is l which is l^*/L^*, and the primary concern is with the properties induced for a short body for which l is small, when the Reynolds number is comparatively large. The body is generally translating upstream

https://doi.org/10.1017/S0956792519000378 Published online by Cambridge University Press

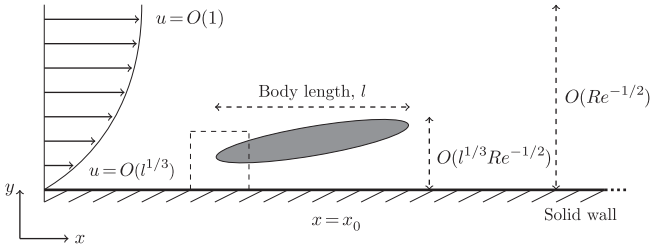


FIGURE 1. Sketch of the small body in a viscous wall layer: this is lying in the depths of a boundary layer of standard $O(Re^{-1/2})$ thickness, or close to a channel or pipe wall. The body is subjected to uniform oncoming shear flow at the bottom of the boundary layer, viscous-inviscid and pressure forces surrounding the body and a small Euler region (dotted) near the leading edge of the body. The typical angle involved is of order $l^{-2/3}Re^{-1/2}$ and l is the body length.

or downstream but only at an assumed slow rate consistent with the fluid velocities in the wall layer (a feature which implies that only high incidence angles of the incoming body motion can affect the local fluid–body interaction). Hence, over the time scales of current interest, the body is present at an effectively constant order-unity distance x_0 say downstream from the airfoil leading edge.

The thin boundary-layer set-up along the undisturbed surface ahead of the near-wall body and also downstream of it is a classical one having x scale of order unity. The boundary-layer approximation is based upon the assumption that the flow Reynolds number is large, in which case the y scale is of order $Re^{-1/2}$, with u, p variations of $O(1)$ and v being of $O(Re^{-1/2})$. The time scale there is of order unity. This boundary layer and its local free stream form the oncoming and surrounding flow field for the body/fluid interactive motion, see Figure 1. The main range of interest is for scaled lengths such that

$$Re^{-3/4} \ll l \ll Re^{-3/8}, \tag{2.1}$$

as described in detail in Appendix A. The range of validity in (2.1) [23, 25] is actually quite a large one in terms of the scales covered. The flow structure at this stage is concentrated primarily in the thin sublayer surrounding the moving body as in Figure 1. The body at an unknown position near the wall occupies the interval $0 < X < 1$ in a frame translating in the positive or negative x-direction slowly streamwise with the body and the body thickness is comparable with the sublayer height. There is a lack of overall displacement over these short length scales [23, 25]. In the sublayer at leading order

$$(u, v, p) = \left(l^{1/3}U, l^{-1/3}Re^{-1/2}V, l^{2/3}P\right), \tag{2.2}$$

with $x - x_0 = lX,\ y = l^{1/3}Re^{-1/2}Y,\ t = \alpha l^{2/3}T$ and where the large constant α is to be determined and the capital-lettered quantities are of order unity. The largeness of α implies that the fluid flow is quasi-steady. By contrast the body motion is unsteady.

Concerning the body motion, the differential pressure forcing due to the fluid flow at the top and under surfaces of the body makes the body move in response. The body motion is controlled by

https://doi.org/10.1017/S0956792519000378 Published online by Cambridge University Press

$$Mh_{TT} = \int_0^1 \left(P^-(X,T) - P^+(X,T)\right) dX, \tag{2.3a}$$

$$I\theta_{TT} = \int_0^1 (X-\beta)\left(P^-(X,T) - P^+(X,T)\right) dX. \tag{2.3b}$$

owing to the rates of change in the normal and angular momenta of the body. The centre of mass of the body is taken at a general position $X = \beta$ while $h(T), \theta(T)$ account for the normal and rotational movement, respectively, of the centre of mass. Herein, the superscripts $\pm$ refer to properties on top of and underneath the body in turn and P denotes scaled pressure due to fluid flow. The mass M^* of the body is equal to $\alpha^2\rho^* L^{*2} l^{8/3} Re^{1/2} M$ with M being of order unity, and likewise the scaled moment of inertia I is $O(1)$. The overall time scale is based on the body motion. As an estimate M^* is approximately $\rho_B^* V^*$ in 2D where ρ_B^* is the density of the body and the effective cross-sectional area V^* is the product of the x and y scales in (2.2) multiplied by L^{*2} through non-dimensionalisation. Hence, α^2 is comparable with $l^{-4/3}\rho_B^*/\rho^*$. This means that the flow behaviour remains quasi-steady provided the density ratio $\rho_B^*/\rho^* \gg l^{4/3}$. With regard to the role of the Re factors in the identification of M^* and the x and y scales, the influence of Re is also inherent in α via the term involving l due to the scaling in (2.1). Since l is small anyway, the theory seems to be valid over a wide range of density ratios. Further in (2.3a) and (2.3b), the $P^{\pm}$ responses are those produced by the fluid flow as described below, thus provoking fluid–body interaction. In the streamwise direction, the body momentum and the relatively small fluid-flow forces are consistent with the body velocity u_c and hence the relative wall velocity U_w being constant.

Concerning the fluid flow, the quasi-steady condensed flow interaction [23, 25] follows from the Navier–Stokes equations, subject to (2.2), giving the governing equations

$$U = \Psi_Y, \ V = -\Psi_X \tag{2.4a}$$

$$UU_X + VU_Y = -P_X(X,T) + U_{YY}. \tag{2.4b}$$

within the gap underneath the body and within the layer above the body. The unknown scaled pressure $P(X,T)$ is independent of Y because of the normal-momentum equation in each layer, such that:

$$P = P^+(X,T), P = P^-(X,T) \text{ above and below the body, respectively,} \tag{2.4c}$$

in keeping with the pressures in (2.3a) and (2.3b). The relevant boundary conditions are

$$U = U_w, \ V = 0 \text{ at } Y = 0, \tag{2.5a}$$

$$U = V = 0 \text{ at } Y = F^-(X,T), \tag{2.5b}$$

$$(U,P) = \left(\lambda Y + U_w + a, \ \frac{U_w^2}{2} - \frac{(U_w+a)^2}{2}\right) \text{ at } X = 0^+, \tag{2.5c}$$

in the gap. The requirements (2.5a) and (2.5b) stem from the no-slip conditions at the wall and on the moving undersurface F^- of the body. The effective streamwise velocity U_w of the wall is

https://doi.org/10.1017/S0956792519000378 Published online by Cambridge University Press

associated with the translation velocity u_c of the body relative to the wall: clearly if the body is translating upstream relative to the wall, then U_w is positive. We should reiterate that U_w being of $O(1)$ corresponds to high incidence angles of the incoming body motion. The conditions in (2.5c) are due to an unknown pressure jump, written

$$P = \pi_2 = \frac{U_w^2}{2} - \frac{(U_w + a)^2}{2},$$

emerging across an Euler region [29] which surrounds the leading edge $X = 0$; a corresponding jump a is induced in the streamwise velocity U to satisfy the quasi-steady Bernoulli balance. The positive $O(1)$ factor λ in (2.5c) is the given scaled incident wall shear stress, namely $Re^{-1/2}(\partial u/\partial y)$ at $y = 0$, in the surrounding boundary layer locally, as in Figure 1 but allowing here for the moving frame. The Euler region is similar to that in [29, 28], its streamwise extent being of order $l^{1/3}Re^{-1/2}$. In the flow on top of the body, by contrast, we have

$$U = V = 0 \text{ at } Y = F^+(X, T), \tag{2.6a}$$

$$U \sim \lambda Y + U_w \text{ as } Y \to \infty, \tag{2.6b}$$

$$(U, P) = (\lambda Y + U_w,\ \lambda a W) \text{ at } X = 0^+. \tag{2.6c}$$

The condition (2.6a) is for no slip on the top moving surface of the body. The function F^+ denotes the unknown scaled position of the body's top surface which is addressed further just below. The requirement (2.6b) of effectively zero displacement in Y corresponds to the feedback effect from the flow outside the sublayer being relatively small. Condition (2.6c) again comes from the Euler jump in pressure,

$$P = \pi_1 = \lambda a W,$$

and in velocity, subject to mass conservation at the body surface; conservation of vorticity is assured because of the local λY variation throughout. The term W is the scaled width of the gap at, or the height of, the leading edge of the body and is in general an unknown function $W = W(T)$ of the scaled time.

The body is translating with a small constant velocity u_c which is assumed to be comparable with the fluid flow velocity in (2.2) and thus gives rise to the scaled wall velocity U_w in the moving frame, where $u_c = -l^{1/3}U_w$. Hence, U_w can be positive or negative. The incident flow at $X = 0^-$ is one of constant shear with a velocity profile $U = \lambda Y + U_w$ for all $Y \geq 0$ and is at zero pressure. The different pressures $P^\pm$ induced above and below the body act to move the body as described earlier. The moving surface shapes $F^\pm$ are given specifically by

$$F^\pm(X, T) = g^\pm(X) + h(T) + (X - \beta)\theta(T), \tag{2.7a}$$

Here, $g^\pm(X)$ are the prescribed solid body shapes, atop and underneath, independent of T, whereas, to repeat, $h(T)$, $\theta(T)$ denote the evolving normal height and azimuthal rotation of the centre of mass of the body. We deal with non-blunt bodies in the sense that $g^\pm$ are equal at $X = 0$, and so $F^\pm$ are equal there, leading to the relation

$$W(T) = h(T) - \beta\theta(T), \tag{2.7b}$$

https://doi.org/10.1017/S0956792519000378 Published online by Cambridge University Press

between W, h, θ. Further here, given that Ψ is zero at the wall, we note also the value

$$\Psi = \lambda W^2/2 + (U_w + a)W, \tag{2.7c}$$

at the under- and top-surfaces of the body from integration of (2.5c) across the gap. This value can be used with (2.5c) and (2.6c) to set the value of the stream function for all Y values at $X = 0^+$. Finally the condition

$$P^+ = P^- \text{ at } X = 1. \tag{2.7d}$$

holds since there can be no pressure difference across the fluid wake behind the body and a Kutta condition of smooth departure of the flow from the trailing edge is imposed.

The fluid–body interaction is governed by the central problem of solving (2.3a)–(2.7d). This is a nonlinear near-wall coupling which involves effects from viscous and inviscid dynamics. The argument has been presented for a boundary-layer setting. A similar setting holds for channel flow and yields the same problem (see Appendix A), with scale ranges different from (2.1). The interaction can also be expressed more broadly in terms of the local incident shear value (e.g. [2]) alone. We note that the fluid-flow part of the present coupling is quasi-steady. The problem posed is nevertheless a difficult numerical one generally for order-unity values of the parameters and length scales involved. Since our interest here is more in initial entry effects, we investigate analytical features below where the concern is with effects occurring for large values of W^* which is a constant parameter representing a typical value of the scaled height $W(T)$.

3 Nonlinear effects at large W^*

Here, we seek to gain analytical insight for cases where the typical scaled body height from the wall is large, so that the gap is enlarged between the lower wall and the body. The flow structure for (2.4a)–(2.7d) is examined next for $W^* \gg 1$, especially in view of the interesting behaviour suggested by the trend in the overbody pressure in (2.6c), while the coupling with the evolving body motion via (2.3a) and (2.3b) is explored in a subsequent section. The main X scale remains of $O(1)$. The body inside the viscous wall layer is sited now at $Y = F^{\pm}(X, T) = W^* Y_0^* + O(1)$, where the constant Y_0^* could be defined as unity but is retained in the working to keep track of the height effect.

When W^* is large we expect four sublayers *I–IV* to occur for the interval $0 < X < 1$ as depicted in Figure 2. Layer *I* is a viscous sublayer near the wall, layer *II* is an essentially inviscid sublayer between the wall and the underbody, while layer *III* is the quasi-inviscid sublayer above the body and layer *IV* represents the comparatively thin viscous sublayers on the body itself. We can also expect the Euler jump conditions to produce merely a displacement of the incident velocity profile $U = \lambda Y + U_w$ for most positive Y values but combined with a large overbody pressure π_1 that is of order W^*,

$$\pi_1 = W^* \pi_1^*, \tag{3.1}$$

say, to leading order: see (2.6c). In contrast, the local gap pressure π_2 is expected to remain $O(1)$. The four sublayers are addressed in turn below.

https://doi.org/10.1017/S0956792519000378 Published online by Cambridge University Press

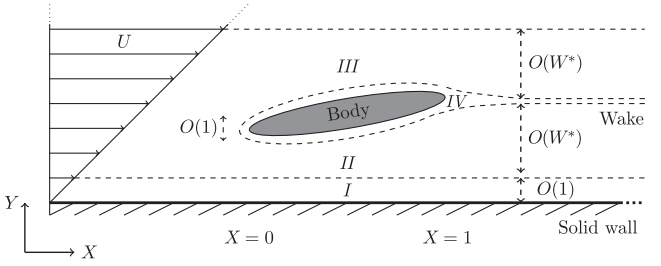


FIGURE 2. Sketch of the body sited near the outer edge of the viscous layer in scaled coordinates. The flow structure surrounding the body for large W^* is shown along with the wake downstream.

Sublayer I has flow quantities of order unity throughout, hence being subjected to the leading order-unity effects from the leading-edge jump directly, such that

$$(U, \Psi, P) = (U^*, \Psi^*, P^*) + ..., \ Y = O(1), \tag{3.2}$$

with $X \sim 1$. It follows that the boundary-layer equations (2.4a) and (2.4b) continue to hold in full for the starred quantities in terms of X, Y. The relevant boundary conditions are

$$U^* = U_w, \ V^* = 0 \text{ at } Y = 0, \tag{3.3a}$$

$$U^* \sim \lambda \left(Y + A_2^*(X, T)\right) + U_w \text{ as } Y \to \infty, \tag{3.3b}$$

$$U^*(\text{at } X = 0^+) = U_2(Y, T) \text{ for all } Y > 0, \ P^*(\text{at } X = 0^+) = \pi_2. \tag{3.3c}$$

where vorticity U_Y is conserved along Euler streamlines, (2.6c) holds and the unknown initial profile $U_2(Y, T) = \lambda Y + U_w + a(T)$ and pressure $\pi_2(T)$ are as in Section 2. The presence of the unknown displacement $A_2^*(X, T)$, which is equal to $a(T)/\lambda$ at $X = 0^+$, is inferred from the large-W response in Section 2 and also anticipates the displacement effect found below in sublayer *II* lying on top of the present sublayer. If we know $\pi_2(T)$, we can determine $a(T)$ and hence $U_2(Y, T)$ for $0 < Y < \infty$ from the Euler jump.

Sublayer II is relatively thick, occupying the gap between the underside of the body and the top of sublayer *I*. In sublayer *II*, we have $Y = W^* Y^*$ with Y^* of order unity. The dominant displacement effect here follows from properties of the Euler zone solution as explained in Section 2. Here, $0 < Y^* < Y_0^*$ and

$$(U, \Psi, P) = (\lambda W^* Y^* + U_2^*, \ \lambda W^{*2} Y^{*2}/2 + W^* \Psi_2^*, \ P_2^*) + ..., \tag{3.4}$$

where the governing equations (2.4a) and (2.4b) together with matching conditions yield the solutions

$$U_2^* = \lambda A_2^*(X, T) + U_w, \tag{3.5a}$$

$$\Psi_2^* = (\lambda A_2^*(X, T) + U_w) Y^*, \tag{3.5b}$$

$$P_2^* = P^*(X, T). \tag{3.5c}$$

https://doi.org/10.1017/S0956792519000378 Published online by Cambridge University Press

The match with the velocity response in sublayer I as Y^*0_+ is as displayed earlier in (3.3b), and tangential flow on approach to the underbody as $Y^* \to Y_0^*$ requires

$$A_2^*(X,T) + U_w/\lambda = -f^-(X,T) - K^-(T). \tag{3.5d}$$

Here, f^- is the scaled underbody shape such that $F^{\pm}(X,T) = W^*Y_0^* + f^{\pm}(X,T)$ and K^- is a function of time to be found representing the unknown change in mass flux into the gap. We take the finite body shape as closed such that $f^+(0,T) = f^-(0,T)$ at the leading edge and similarly $f^+(1,T) = f^-(1,T)$ at the trailing edge.

Sublayer III lies above the body, again with X of $O(1)$. The expansion now has the form

$$(U,\Psi,P) = (\lambda W^*Y^* + U_1^*,\ \lambda W^{*2}Y^{*2}/2 + W^*\Psi_1^*,\ W^*P_1^*) + ..., \tag{3.6}$$

which holds for order-unity values of $Y^* > Y_0^*$. We notice that the displacement is $O(1)$ in *III*, namely $-A_1^*$ as described below, whereas the pressure has been raised (to combat the displacement over the present enlarged gap in effect, given that the overall displacement must be zero from (2.6b)) to order W^* in keeping with the trend (3.1). The controlling equations here are

$$U_1^* = \frac{\partial \Psi_1^*}{\partial Y^*}, \tag{3.7a}$$

$$\lambda Y^* \left(\frac{\partial U_1^*}{\partial X}\right) - \left(\frac{\partial \Psi_1^*}{\partial X}\right)\lambda = -\frac{\partial P_1^*}{\partial X} \tag{3.7b}$$

from substitution into (2.4a) and (2.4b). The presence of the pressure gradient in the streamwise momentum balance at leading order is noteworthy as it contrasts with the balance holding in the sublayer *II* between the underbody and the wall. The solution in *III* is

$$U_1^* = \lambda A_1^*(X,T) + U_w, \tag{3.8a}$$

$$\Psi_1^* = (\lambda A_1^*(X,T) + U_w)Y^* + P_1^*/\lambda. \tag{3.8b}$$

The absence of an additional constant in (3.8b) is due to matching with (2.6c) as X tends to 0^+, given the surface value in (2.7c). The boundary condition (2.6b) however requires zero displacement, and the condition (2.6a) on the overbody leads to a constraint on the pressure, leaving us with

$$A_1^*(X,T) = 0, \tag{3.8c}$$

$$P_1^*(X,T) = \lambda^2 Y_0^*(f^+(0^+,T) - f^+(X,T)) + \pi_1^*(T), \tag{3.8d}$$

bearing in mind that we expect the starting value $P_1^*(0^+,T) = \pi_1^*(T)$ because of the jump conditions. The original displacement function expands in the form $A_1^* + ...$ over the present length scale, thus giving the result (3.8c). Despite the negligible displacement, a significant normal velocity is induced above the body because of the presence of the pressure gradient.

Sublayer IV consists of attached Blasius layers, one on each side of the body. Their thickness is much less than that of the body and their influence on the current interactions is negligible.

The results above hold throughout $0 < X < 1$. Also the $O(W^*)$ pressure in sublayer *III* is significantly greater than the pressure in sublayer *II*. Combining the results of sublayers *II*,

https://doi.org/10.1017/S0956792519000378 Published online by Cambridge University Press

III and equating the values of the stream function Ψ on the underbody and the overbody to conserve mass produces the following expression for the displacement effect acting on the lowest sublayer *I*,

$$A_2^*(X,T) = (f^-(0^+,T) - f^-(X,T)) + \pi_1^*(T)/(\lambda^2 Y_0^*). \tag{3.9}$$

The result (3.9) determines the displacement that helps to drive the flow in the lowermost viscous layer *I* by means of the condition (3.3b) but subject to a guessed value of π_1^* and the prescribed Y_0^* value for the leading-edge height. The result (3.9) when applied at $X = 0^+$ also confirms that, in (3.1), the coefficient

$$\pi_1^*(T) = \lambda^2 A_2^*(0^+,T), \tag{3.10}$$

with $Y_0^* = 1$. Since $\lambda A_2^*(0^+,T) = a$, the earlier behaviour in (2.6c) ties in with this coefficient. At the present stage, there is in effect only one unknown, $\pi_1^*(T)$. The required single condition to determine it stems from the trailing-edge condition (2.7d). This now takes the form

$$\pi_1^*(T) = \lambda^2 Y_0^*(f^+(1,T) - f^+(0^+,T)), \tag{3.11}$$

in order to make $P_1^*(1,T)$ be zero, since the pressure on the overbody greatly exceeds that on the underbody in view of (3.4) and (3.6). Hence, the overbody pressure in (3.8d) becomes

$$P_1^*(X,T) = \lambda^2 Y_0^*(f^+(1,T) - f^+(X,T)), \tag{3.12}$$

and the displacement is simply given by

$$A_2^*(X,T) = f^-(1,T) - f^-(X,T). \tag{3.13}$$

The implications are examined in the following sections for steady flow and then for unsteady flow.

4 Implications in steady flow

We divide the description of steady flows, where the body shape and orientation are assumed given, into broader-scale properties and near-wall properties. These are addressed in Subsections 4.1 and 4.2, respectively, below. The scaled time derivatives in T may be omitted for convenience.

4.1 Solutions for overbody pressure and underbody displacement

Here, we may use the results (3.12) and (3.13) directly. The finding (3.12) is a remarkably simple and explicit finding, showing the scaled pressure which acts on top of the body to be directly proportional to the prescribed shape function of the top surface of the body (the overbody). The reason for this lies in the outer boundary condition on the viscous wall-layer flow which requires an overall displacement effect of zero there and hence leads to a severe confinement and acceleration or deceleration of the fluid flow above the body in a quasi-inviscid fashion (this result is equivalent to having one-dimensional inviscid flow present). The underbody shape has

https://doi.org/10.1017/S0956792519000378 Published online by Cambridge University Press

no impact here. The resultant expressions for the lift force C_L and moment C_M acting on the body are, respectively:

$$C_L = a_1 \int_0^1 \left(f^+(X) - f^+(1)\right) dX, \tag{4.1a}$$

$$C_M = a_1 \int_0^1 (X - \beta) \left(f^+(X) - f^+(1)\right) dX. \tag{4.1b}$$

in scaled terms, where $a_1 = W^* \lambda^2 Y_0^*$ is a positive constant. It is notable that these expressions are dominated by the contribution from the top pressure and they form the right-hand sides of the body-motion equations (2.3a) and (2.3b). Despite the simplicity mentioned above however general rules are not so simple to deduce as regards the lift and moment. The lift C_L is proportional to the area under the curve formed by the overbody shape function but with that curve moved normally to give zero at the trailing edge $X = 1$. Hence referring to (2.7a) the height factor h has no influence on the lift in the present regime, while a positive/negative angle θ contributes a negative/positive lift. We can see also that an overbody shape which is nose-up (meaning $f^+(0)$ is positive) and of convex shape yields positive lift and the same is true if the overbody is straight or not especially concave. Conversely, a nose-down concave shape yields negative lift, i.e. positive downwash, as does a straight or not especially convex shape if nose-down. On the other hand, more involved shapes could reverse those lift values. Similar trends apply to the moment C_M: here again h has no influence whereas the contribution from θ is $a_1\theta(3\beta - 1)/6$ which may be of either sign.

Apart from those observations, the clearest way to gain some further insight seems to be through specific examples. Figure 3 presents results for the parabolic overbody shape

$$f^+ = b_1 X + b_2 X(1 - X). \tag{4.2}$$

Here, C_L, C_M are plotted against b_1 for given values of b_2, β. The results show that C_L, C_M can both be negative for a range of b_1 values but at sufficiently large positive b_2 both become positive, thereby yielding trends towards upthrust and anticlockwise rotation for the body at increased negative incidence (the nose-down attitude). Figure 4 gives plots of C_L, C_M for the elliptical shape

$$f^+ = b_3 X + b_4 X^{1/2}(1 - X)^{1/2}, \tag{4.3}$$

with b_4 being varied for prescribed b_3, β values. Again we see interesting trends including positive and negative lift and moment as the parameters are varied. Solutions for a flexible body whose shape is coupled with the flow pressure are discussed in Appendix B. The predictions for lift and moment are used in Section 5 to determine the motion of the body. The predicted underbody displacement (3.13), which is likewise quite simple and explicit in terms of the given underbody shape rather than the overbody shape, is used in the next subsection to determine the wall-layer response and the gap pressure.

https://doi.org/10.1017/S0956792519000378 Published online by Cambridge University Press

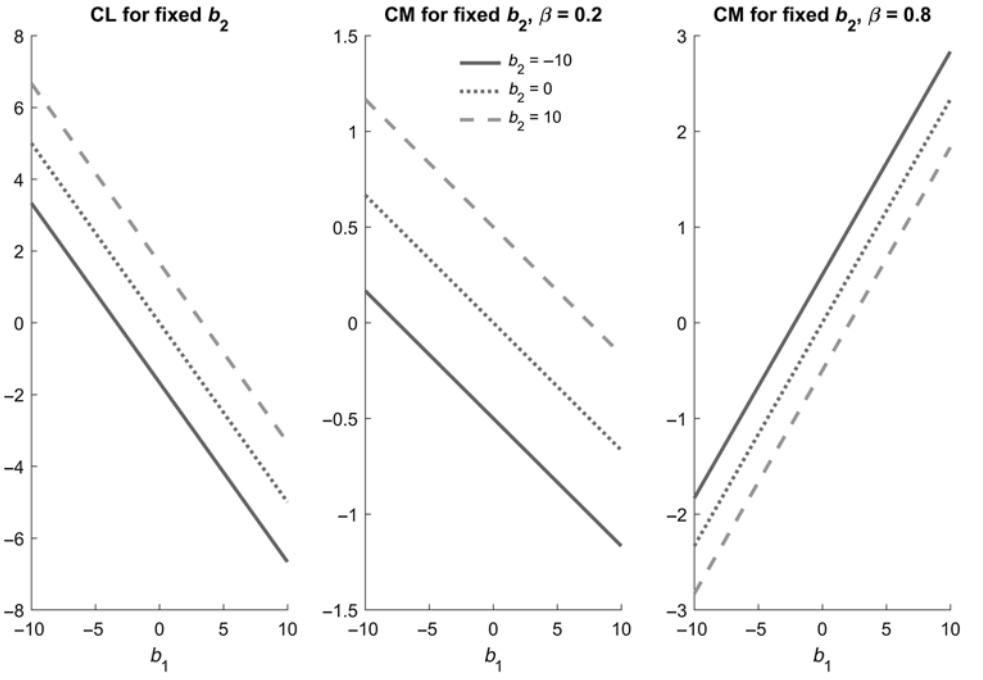


FIGURE 3. Dependence of scaled lift and moment C_L, C_M on shape factors b_1, b_2 for different β values, in the case of a parabolic shape of overbody (note: C_L is independent of β).

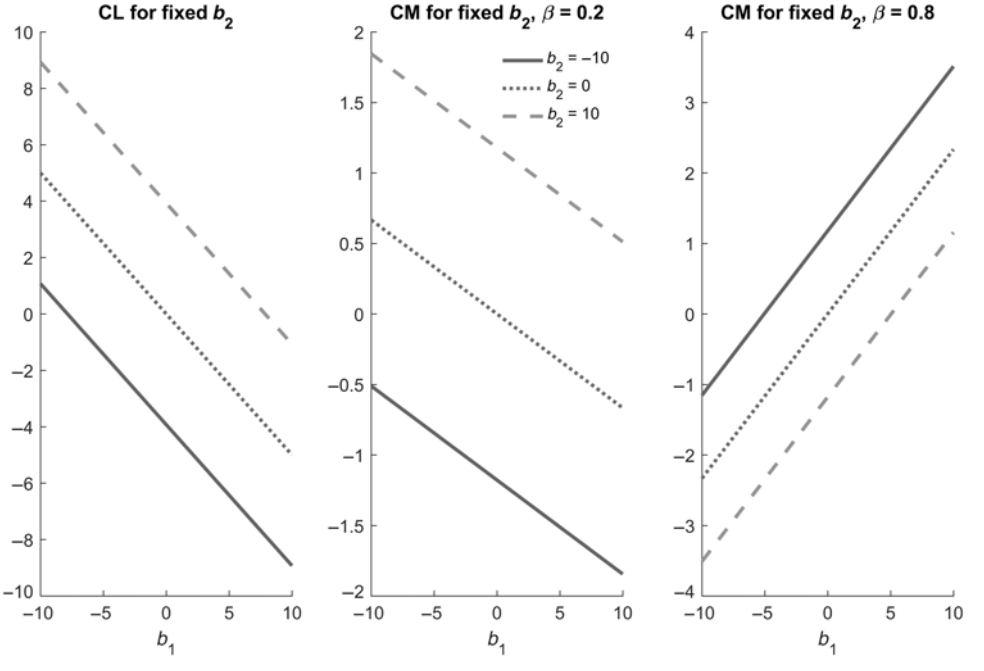


FIGURE 4. As in Figure 3 for an elliptic shape (note: C_L is independent of β).

https://doi.org/10.1017/S0956792519000378 Published online by Cambridge University Press

4.2 Underbody and wall pressure, wall shear stress, separation

The near-wall properties of interest are governed by the features of the sublayer I of Section 3, concerning nonlinear interaction associated with the wall-layer equations (2.4a) and (2.4b) with (U, Ψ, P) replaced by (U^*, Ψ^*, P^*) subject to the boundary conditions in (3.3a)–(3.3c). Here, the given displacement A_2^* is prescribed by (3.13) whereas the scaled pressure P^* is to be found, giving the underbody pressure and the wall pressure since P^* is independent of the normal coordinate. It is interesting that, in contrast with the problems addressed by [27, 24], the current wall-layer problem requires only a single march forward in the streamwise direction subject to the prescribed displacement of (3.13). The resulting pressure P^* produced at the trailing edge acts merely to afford a slight correction to the trailing-edge condition of (3.11).

A numerical treatment is necessary in general for the wall-layer calculation. We used finite differencing based on a semi-implicit scheme whereby at each X station the scheme iterates for the P^* value in order to satisfy all the boundary conditions in the normal direction. As in [32], a double-stepping procedure is adopted to achieve second-order accuracy. Since the analysis for small positive X indicates that locally a Blasius-like thin layer arises at the wall, a transformation $X \to X^{1/2}$ was applied to render the relevant local normal coordinate linear in the transformed X coordinate and then a sufficiently fine normal discrete step δY was taken to capture the Blasius-like local forms. Streamwise marching forward in X then followed successively: here and above we assumed forward flow initially but the scheme was able to cope with comparatively small flow reversals by means of a Flare approximation [1]. The scheme sets the small spatial steps δX, δY such that typically 401 points were used in the streamwise direction and 401 normally. Finite grid effects were tested by varying these steps and examining the changes to the solutions obtained, indicating that the results shown here are accurate to within a 1% error in pressure typically.

The results shown in Figures 5–7 are focussed on cases highlighting the main influences of body orientation, body thickness and relative streamwise velocity of the wall. The specific underbody body shape considered is given by

$$f^- = c_1 X + c_2 X(1 - X), \tag{4.4}$$

with A_2^* then following from (3.13). Here, c_1, c_2 are prescribed constants. The c_1 term corresponds broadly to the scaled angle θ, whereas the curvature term c_2 provides an influence from body thickness. Taking c_1 negative would make A_2^* be negative at $X = 0^+$, indicating a considerable flow reversal ahead of the body, and so we keep c_1 non-negative. Adding a constant to the right-hand side of (4.4) to represent a uniform shift in gap width or height would have no effect on A_2^*. The incident wall shear λ can be normalised to unity without loss of generality. We thus have a three-parameter set (U_w, c_1, c_2) to consider. Figure 5(a), (b) shows solutions for four cases $(0, c_1, 0)$ as the effective angle c_1 is varied from 0.1 to 16. As c_1 is increased, the typical magnitude of both the induced pressure P^* and the wall shear stress $\partial U^*/\partial Y$ at $Y = 0$ increases substantially. Figure 5(b) provides a close-up view for small c_1 which is discussed more in the next paragraph. In Figure 5(a), the pressure gradient is sufficiently adverse for the larger c_1 angles that flow separation in the sense of flow reversal (beginning when the wall shear stress becomes negative) is encountered, with the separation point moving upstream. The limiting separation point shown by a thick arrow in the figure is implied by the analysis presented in the next-but-one paragraph. Figure 6 gives results for $(1, 1, c_2)$ cases with the thickness parameter c_2 being

https://doi.org/10.1017/S0956792519000378 Published online by Cambridge University Press

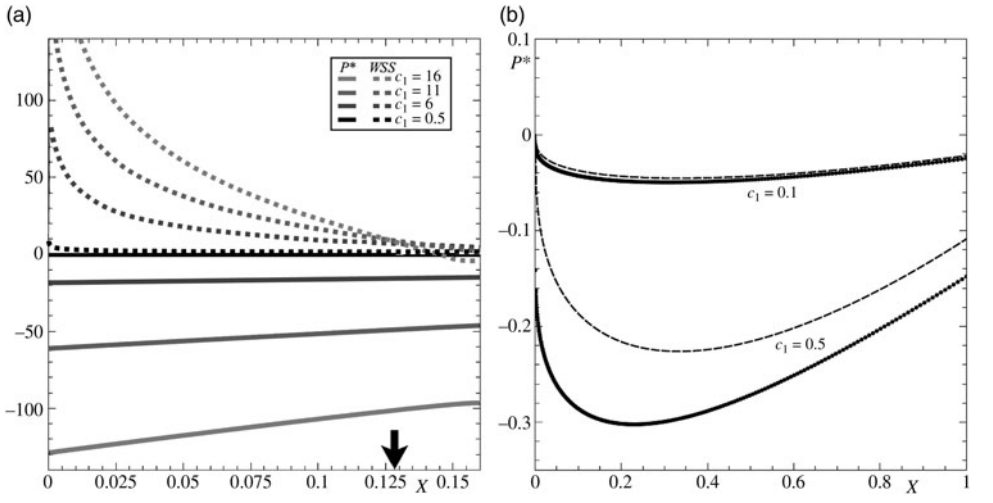


FIGURE 5. (a) Plots of wall shear stress and wall pressure P^* under the body versus X for cases $(U_W, c_1, c_2) = (0, c_1, 0)$ with $c_1 = 0.5, 6, 11, 16$. The thick downward arrow indicates the limiting position of the separation point for large c_1, based on Figure 8 below. (b) As (a) but for $c_1 = 0.1, 0.5$ (solid curves) together with linearised-theory results (dashed) for comparison.

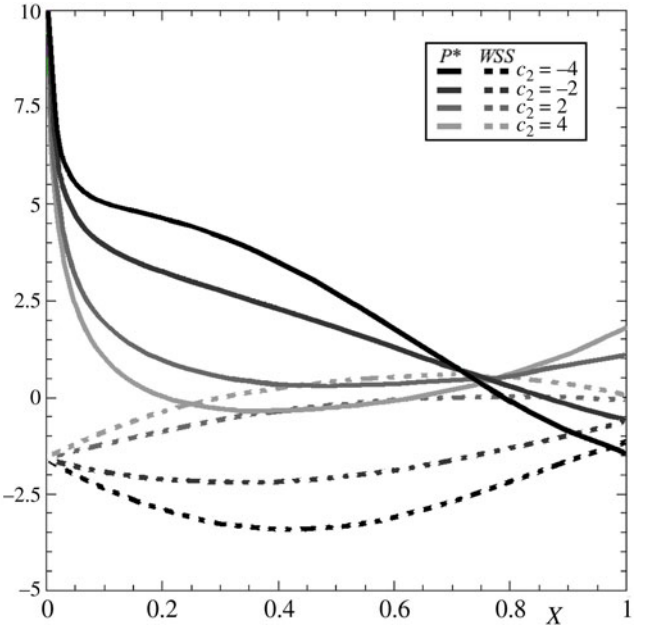


FIGURE 6. Wall shear stress and wall pressure P^* for cases $(U_W, c_1, c_2) = (1, 1, c_2)$ with $c_2 = -4, -2, 2, 4$.

varied from -4 to 4. Here, no significant flow reversal occurs: the wall shear stress becomes negative in some instances but the downstream moving wall continues to draw all the fluid forward. When c_2 becomes more negative, which is associated with the underbody being increasingly convex relative to the wall (hence the gap narrows), the variation in pressure and wall shear stress

https://doi.org/10.1017/S0956792519000378 Published online by Cambridge University Press

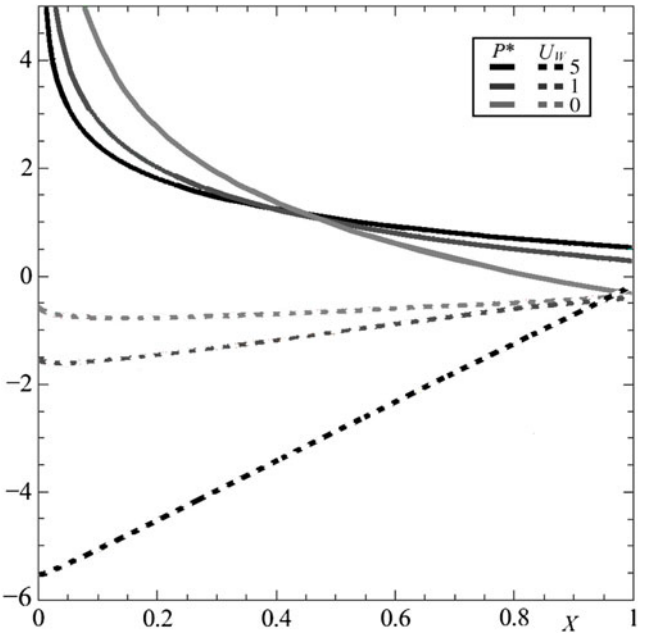


FIGURE 7. Wall shear stress and wall pressure P^* for $(U_W, c_1, c_2) = (U_W, 1, 0)$ with $U_W = 0, 1, 5$.

increases notably. Figure 7 presents results for $(U_w, 1, 0)$ cases. As U_w is increased from zero, the magnitude of the pressure and wall shear stress variations again increases and in particular a significant adverse pressure gradient appears.

Certain extremes of interest can now be investigated analytically. First, if f^- is small (corresponding to c_1, c_2 being small in the case of (4.4)), then A_2^* is small from (3.13) and so a linearised solution of the sublayer problem applies. For zero U_w, this yields the explicit relation

$$P^*(X) = -\gamma \int_0^X \left(f^-(1) - f^-(S)\right)(X-S)^{-2/3} dS, \tag{4.5}$$

determining [18] the induced wall pressure for a given underbody shape $f^-(X)$. The constant $\gamma = 0.289838\lambda^{5/3}$ is positive. Comparisons between the prediction (4.5) and the earlier numerical predictions are given in Figure 5(b) for the case of zero U_w, c_2: the analytical prediction and the numerical prediction are much closer to each other for c_1 of 0.1 than for c_1 of 0.5 and indicate fair agreement.

Second, suppose for generality that all of U_w, c_1, c_2 are large and the streamwise scale X remains of $O(1)$. Then A_2^* is large, say of order α, and so we expect U^* also to be $O(\alpha)$ in view of (3.3b). The momentum balance in (2.4b) therefore suggests that P^* is $O(\alpha^2)$ and that Y becomes of order $\alpha^{-1/2}$ in order to preserve the viscous-inviscid balance. Thus, the expansion

$$\begin{aligned} &(U^*, A_2^*, f^-, U_w) = \alpha(\bar{U}^*, \bar{A}_2^*, \bar{f}^-, \bar{U}_w) + \ldots, \\ &P^* = \alpha^2 \bar{P}^* + \ldots, \; X = O(1), \; Y = \alpha^{-1/2}\bar{Y}, \end{aligned} \tag{4.6}$$

https://doi.org/10.1017/S0956792519000378 Published online by Cambridge University Press

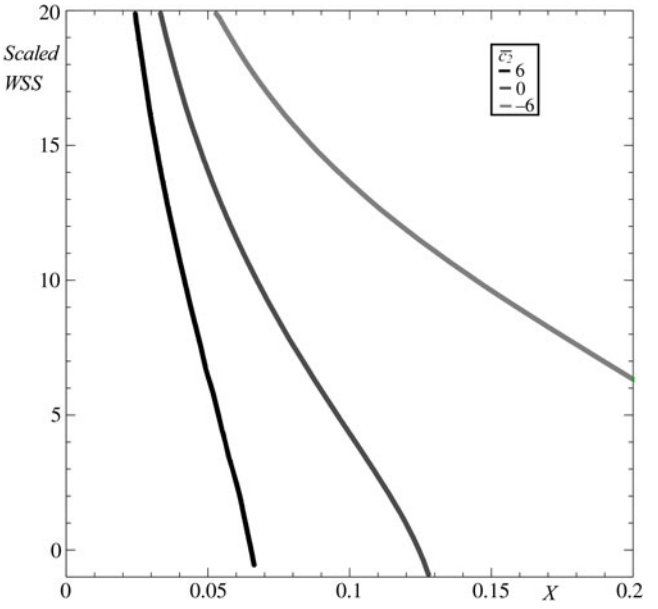


FIGURE 8. Scaled wall shear stress for large α. Here, $\bar{U}_W = 0, \bar{c}_1 = 6, \bar{c}_2 = -6, 0, 6$.

is suggested. Substituting into (2.4a) and (2.4b) yields the wall-layer equations for $\bar{U}^*$, $\bar{\Psi}^*$, namely

$$\bar{U}^* = \bar{\Psi}^*_{\bar{Y}}, \tag{4.7a}$$

$$\bar{V}^* = -\bar{\Psi}^*_{X}, \tag{4.7b}$$

$$\bar{U}^*\bar{U}^*_X + \bar{V}^*\bar{U}^*_{\bar{Y}} = -\bar{P}^*_X(X) + \bar{U}^*_{\bar{Y}\bar{Y}}. \tag{4.7c}$$

but subject to the boundary conditions, from (3.3a)–(3.3c) with (3.13),

$$\bar{U}^* \to \lambda\bar{A}^*_2(X) + \bar{U}_w \text{ as } \bar{Y} \to \infty, \tag{4.7d}$$

$$\bar{A}^*_2(X) = \bar{f}^-(1) - \bar{f}^-(X), \tag{4.7e}$$

$$\bar{U}^* = \bar{U}_w, \bar{\Psi}^* = 0 \text{ at } \bar{Y} = 0, \tag{4.7f}$$

$$\bar{U}^* = \lambda\bar{A}^*_2(0) + \bar{U}_w \text{ at } X = 0^+. \tag{4.7g}$$

Here, the outstanding point [25] is that the wall layer becomes a classical boundary layer because of the loss of the shear contribution λY in (3.3b). The pressure is known in advance of the wall-layer calculation since from (4.7c) at large $\bar{Y}$ coupled with (4.7d) and followed by an integration in X we obtain the result

$$P^* = \bar{U}_w^2/2 - (\bar{U}_w + \lambda\bar{A}^*_2(X))^2/2. \tag{4.7h}$$

The solution of the classical problem (4.7a)–(4.7h) is presented in Figure 8 for the example corresponding to (4.4) with $\bar{c}_1 = 6$ while $\bar{c}_2$ takes the values $-6, 0, 6$ to indicate the influence of thickness and $\bar{U}_w$ is zero. When $\bar{c}_2$ is -6, the relatively narrowed gap leads to enhanced

https://doi.org/10.1017/S0956792519000378 Published online by Cambridge University Press

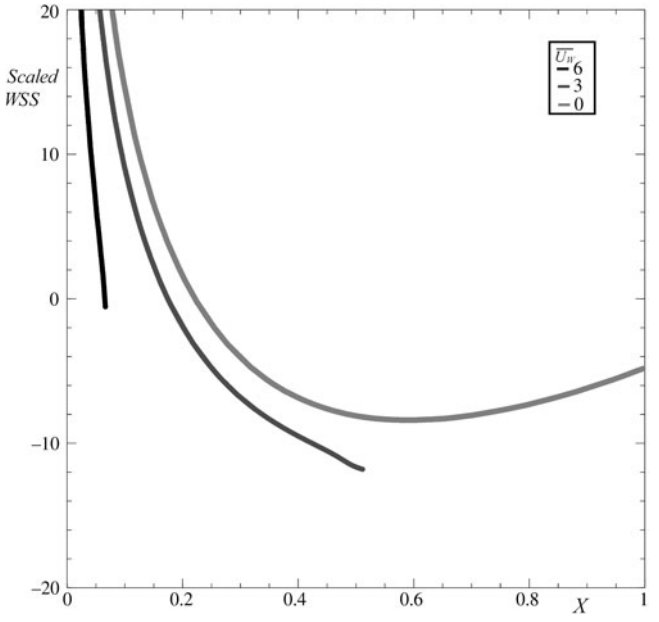


FIGURE 9. As in Figure 8 but $\bar{U}_W = 0, 3, 6, \bar{c}_1 = 6, \bar{c}_2 = 6$.

through-flow and hence enhanced wall shear stress, while in the example of $\bar{c}_2$ equal to 6 the opposite holds with the gap becoming wider and the wall shear stress being reduced, forcing a comparatively early separation to take place. In the example of zero $\bar{c}_2$ the value of $\bar{c}_1$ could be normalised to unity but we kept it at 6 for the sake of comparison. The problem here is similar to that in [25] except for the jump start in (4.7g). The classical form produces a Goldstein singularity in the wall shear stress at a finite value $X = X_{sep}$ (approximately $X_{sep} = 0.128$ for the above example where $\bar{c}_2$ is zero) but local analysis then smooths out the singularity and leads on into an open separation persisting for $O(1)$ values of X downstream of X_{sep}. The separation point X_{sep} predicted for large α lies reasonably close to those in the original numerical results as shown in Figure 5(a) for the cases $(U_w, c_1, c_2) = (0, c_1, 0)$ as c_1 increases. The limiting analysis also confirms via Figure 8 the solution trends for increasing c_2 seen earlier. Figure 9 shows solutions $(\bar{U}_w, 6, 6)$ for increasing $\bar{U}_w$: the $\bar{U}_w$ value of 3 delays the onset of reversed flow compared with the earlier zero value whereas 6 produces fully forward flow all the way from the leading to the trailing edge. The solutions are again in keeping with the earlier results (see Figure 7). Moreover, larger $\bar{U}_w$ leads to a jet-like velocity profile in the sublayer.

5 Implications in unsteady fluid–body interaction

Here, we use the results (3.12), (3.13) together with (2.3a) and (2.3b), with unsteadiness re-admitted. Since the overbody pressure is far greater than the underbody and since a constant shift $W^* Y_0^*$ can be absorbed into h, we obtain the ordinary differential equation

$$Mh_{TT} = -\int_0^1 \lambda^2 Y_0^* \left[g^+(1) - g^+(X) + (1 - X)\theta(T)\right] dX, \tag{5.1}$$

https://doi.org/10.1017/S0956792519000378 Published online by Cambridge University Press

from (2.3a) with (4.1a). Similarly, (2.3b) with (4.1b) leads to the differential equation

$$I\theta_{TT} = -\int_0^1 \lambda^2 Y_0^*(X-\beta)\left[g^+(1)-g^+(X)+(1-X)\theta(T)\right]dX. \tag{5.2}$$

Thus, (5.2) acts to determine $\theta(T)$, while (5.1) then determines $h(T)$ subsequently. We examine next two particular overbody shapes $g^+(X)$ akin to those in (4.2) and (4.3).

The first overbody shape considered is the parabola

$$g^+(X) = C_1X + C_2X(1-X), \tag{5.3a}$$

where C_1, C_2 are given constants. This gives

$$\theta_{TT} = -\frac{\lambda^2 Y_0^*}{6I}(C_1(\beta-1/2)+C_2(1-3\beta)) - \frac{\lambda^2 Y_0^*}{6I}[1-3\beta]\theta(T). \tag{5.3b}$$

Letting $B_1 = -\frac{\lambda^2 Y_0^*}{6I}(C_1(\beta-1/2)+C_2(1-3\beta)), B_2 = |\frac{\lambda^2 Y_0^*}{6I}[1-3\beta]|$, we see that if $\beta > 1/3$ then the exponential form

$$\theta(T) = -\frac{B_1}{B_2} + k_1\exp(T\sqrt{B_2}) + k_2\exp(-T\sqrt{B_2}), \tag{5.3c}$$

holds, where the constants k_1, k_2 are dependent on the initial conditions. Hence from (4.3), the $h(T)$ solution is

$$h(T) = \left(B_4/2 - \frac{B_1B_3}{2B_2}\right)T^2 + \frac{B_3}{B_2}\left(k_1\exp(T\sqrt{B_2}) + k_2\exp(-T\sqrt{B_2})\right) + k_3T + k_4, \tag{5.3d}$$

where B_3, B_4 are known constants, whereas the constants k_3, k_4 are determined by initialisation. Otherwise, if $\beta < 1/3$, the form of $\theta(T), h(T)$ becomes

$$\theta(T) = \frac{B_1}{B_2} + k_1\sin(T\sqrt{B_2}) + k_2\cos(T\sqrt{B_2}), \tag{5.3e}$$

$$h(T) = \frac{B_4}{2} + \frac{B_1B_3}{2B_2}T^2 - \frac{B_3}{B_2}(k_1\sin(T\sqrt{B_2}) + k_2\cos(T\sqrt{B_2}) + k_3T + k_4. \tag{5.3f}$$

Here, the constants k_1, k_2, k_3, k_4 are again dependent on the initialisation.

The second overbody shape considered is that of an ellipse, with prescribed constants C_3, C_4, such that

$$g^+(X) = C_3X + C_4(X(1-X))^{1/2}, \tag{5.4a}$$

which leads to the relation

$$\theta_{TT} = -\frac{\pi\lambda^2 Y_0^*}{I}\left(\frac{C_3}{6}(1-3\beta) + \frac{C_4\pi}{8}\left(\beta-\frac{1}{2}\right)\right) - \frac{\lambda^2 Y_0^*}{6I}\left[1-3\beta\right]\theta(T). \tag{5.5a}$$

The results then follow in basically the same manner as in (5.3b)–(5.3f). Solutions are presented in Figures 10–13. They show the evolution of $h(T), \theta(T)$ for the quadratic overbody at β values of 0.8, 0.2, in Figures 10 and 11, respectively, and then for the elliptical overbody in Figures 12 and 13 for the same two β values in turn. The main finding here is that if $\beta > 1/3$ then exponential growth (instability) arises in θ and hence in h from (5.1), whereas if $\beta < 1/3$, so that

https://doi.org/10.1017/S0956792519000378 Published online by Cambridge University Press

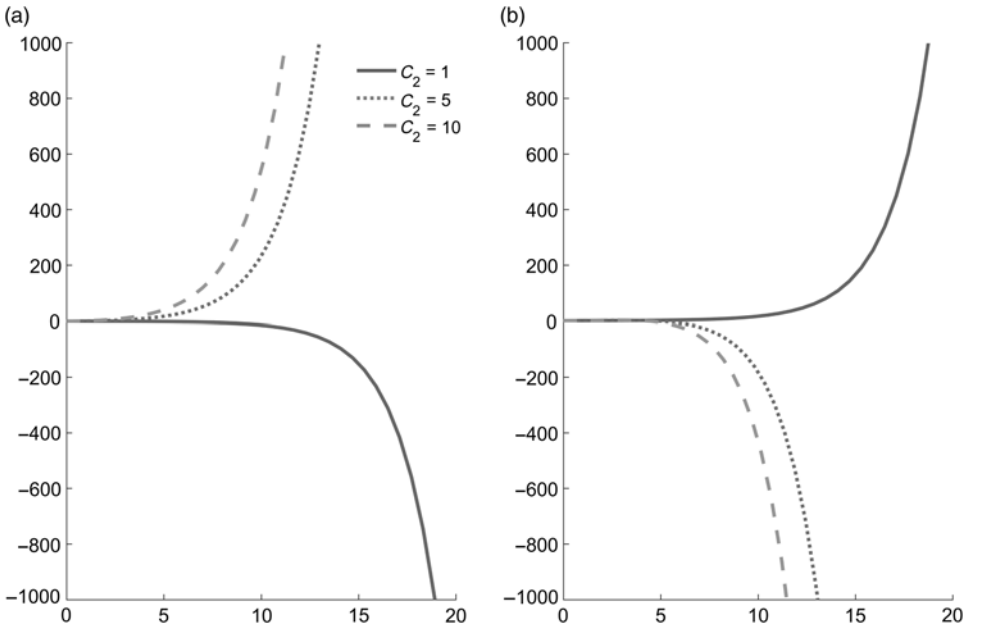


FIGURE 10. Plots of (a) θ, (b) h against scaled time for a parabolic shape when $\beta = 0.8$ with $C_1 = 1$, varying the coefficient C_2.

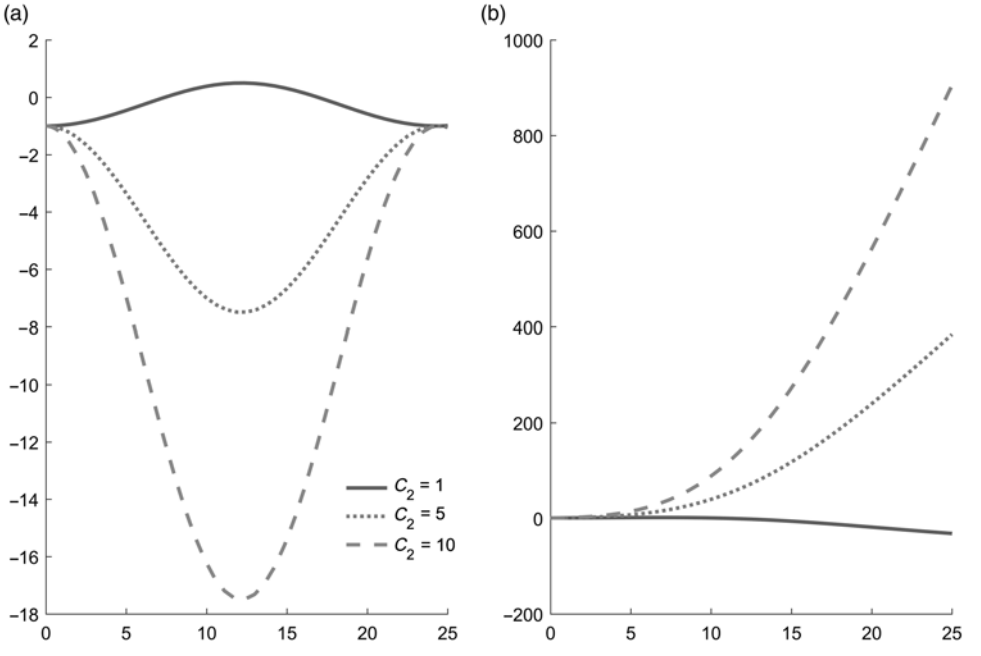


FIGURE 11. Plots of (a) θ, (b) h against scaled time for a parabolic shape when $\beta = 0.2$ with $C_1 = 1$, varying the coefficient C_2.

https://doi.org/10.1017/S0956792519000378 Published online by Cambridge University Press

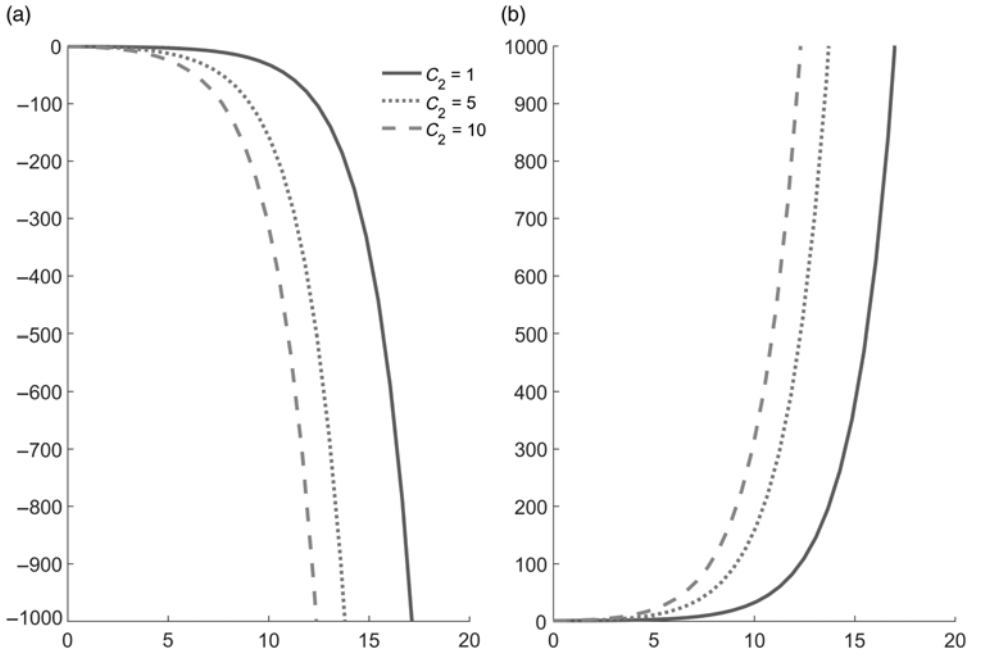


FIGURE 12. Plots of (a) θ, (b) h against scaled time for an elliptic shape when $\beta = 0.8$ with $C_1 = 1$, varying the coefficient C_2.

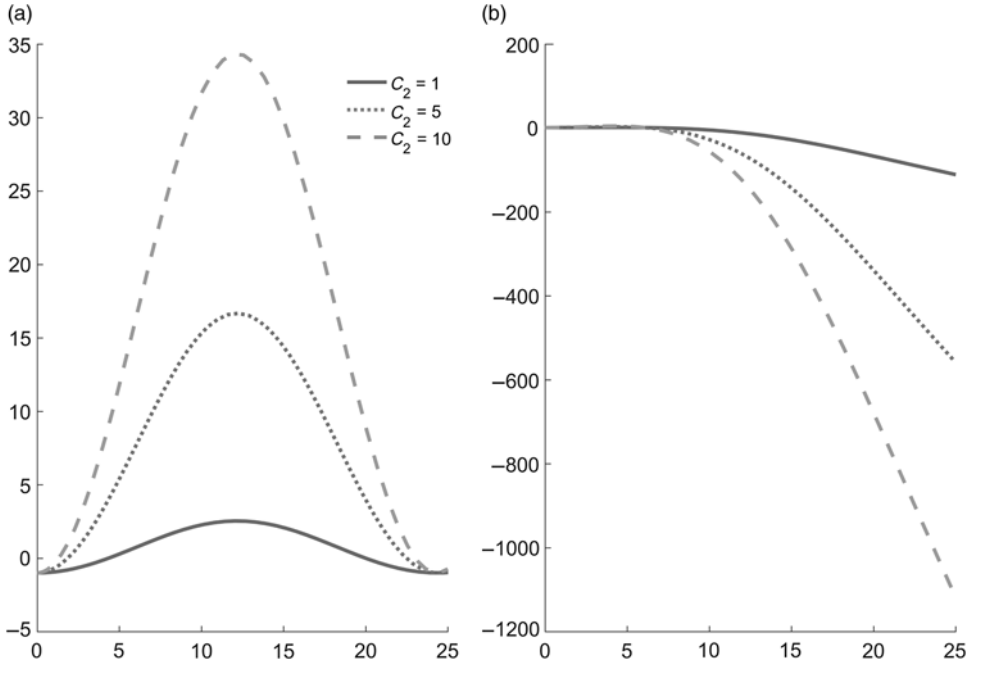


FIGURE 13. Plots of (a) θ, (b) h against scaled time for a elliptic shape when $\beta = 0.2$ with $C_1 = 1$, varying the coefficient C_2.

https://doi.org/10.1017/S0956792519000378 Published online by Cambridge University Press

the centre of mass lies ahead of the midpoint of the body, then periodic oscillations occur in θ, while h grows only linearly with time. Clearly when instability exists it is dictated by the θ_{TT} and θ terms in (5.2). This feature implies that for the calculation of growth rates for any shape of body it is sufficient to address the case of the flat-plate shape, as in [27]. Also the change from instability to potential stability suggested by displacing the centre of mass upstream sufficiently is notable. Stability which is possible for $\beta < 1/3$ is associated with the body remaining in oscillatory motion for a considerable amount of time, departing from such a state only gradually as $h(T)$ increases or decreases linearly in time. Instability for $\beta > 1/3$ corresponds to a much swifter departure from equilibrium, with the body either being ejected away from the wall towards the central parts of the surrounding boundary-layer flow or being attracted towards the wall and entering the strongly nonlinear stage of (2.3a)–(2.7d) in full.

6 Conclusions

Inserting a freely moving body of small but finite size into the outer edge of a viscous wall layer has been found to change the structure of the flow solution considerably, including the whole of the area between the body and the wall. In our case, this has led to a region of comparatively strong pressure being set up above the body which is controlled by linear dynamics, whereas the region below the body, in the gap between the undersurface and the wall, involves nonlinear inertial forces generally despite the lower amplitude of the pressure in the gap. The dominance of the upper pressure acting over the body yields a remarkably simple linear form for the evolution of the body position and its rotation and this leads to interesting phenomena. The unsteady movement of the body can be summarised as yielding either an exponential departure from the outer edge layer as time increases or a continued oscillation within that layer (accompanied usually by a slow departure), depending on the location of the centre of mass of the body.

The body motion also determines the flow-displacement effect explicitly below the body, which acts on the wall vorticity to induce the wall pressure response in a nonlinear fashion. The wall pressure acts across the gap only as a slight correction in terms of the body movement itself. The interaction near the wall is through the nonlinear viscous-inviscid wall layer coupled with the trailing-edge condition which forces the effective displacement to be nonzero at the leading edge, giving a jump effect there. Increasing body thickness, orientation or streamwise movement is found to lead to an enhanced pressure response as well as an enhancement of the wall shear stress over a significant portion of the gap length. Beyond that portion however flow separation may occur, depending on the scaled parameter values involved.

Thus, the main findings are that explicit solutions are obtainable for the movements of the body, separation of the fluid flow near the wall is possible and instabilities can occur over any short length scale of the body. In addition, we have viscous and inertial effects applying at leading order throughout much of the fluid–body interaction. Lubrication effects could still matter however, if the body is situated closer to the wall. The wall considered lies at the bottom of a boundary layer or forms one of the walls in a channel or pipe.

Addressing the issue of practical relevance, we may comment as follows. Given the many motivations described in the introduction, it may be rather surprising that little modelling of an applied-mathematical nature has been done previously in the subject of fluid–body interactions. It was felt by us to be desirable to try starting to fill that gap despite any apparent complexity in the subject. Our intent has been to make a beginning, then, to tackle basic problems and to seek

https://doi.org/10.1017/S0956792519000378 Published online by Cambridge University Press

analytical guidance above all. We have found that complexity or at least delicacy does indeed arise in the study: in the present case of a detached body entering a viscous-inviscid wall layer several important subregions come into play. On the other hand, concise analytical solutions have been derived for the combined fluid–body motion, including influences of body position, thickness and length, and these findings can guide further study. In terms of practical examples, we still need to be cautious, we cannot be sure yet if practical use will ensue and we should not pretend that all regimes mentioned or not mentioned here are likely to be of practical relevance. Nevertheless, let us address a range of Reynolds numbers Re, say 10^4–10^6 depending on the specific airfoil application in mind here, and apply the theoretical scalings. Take W^* to be 2 for example. Then the boundary-layer thickness is about 10^{-3} to 3×10^{-2} and the body length considered is formally about 10^{-3}–10^{-2} (from the range (2.1)) relative to the chord width of unity, while the body thickness is in the approximate range 10^{-3}–10^{-4} (from the scales in (2.2)), as is the wall-layer thickness. Laterally, the body placement on entry to the viscous-inviscid wall layer is at a distance lying between 2×10^{-4} and 2×10^3 from the wall. Overall this theoretical configuration seems reasonably close to some of those described in the introduction relevant to an ice crystal, shard or other thin particle in airfoil and aeroengine dynamics. Similar considerations and estimates apply in a channel flow as described by [31].

Concerning further details on parameters, it has been found that an increase in the underbody shaping through increased underbody thickness and/or orientation angle parameters produces a considerable rise in the amplitude of the pressure response under the body, as shown in Section 4. This raised underbody pressure could eventually counteract the high-amplitude upper pressure, although the body then would be quite unusual in shape by having more bulk underneath than on top. The present study has generally kept the scaled orientation parameter c_1 of order unity and positive and, similarly, the scaled wall velocity (relative to the body) positive or zero as regards the underbody flow. This feature has also avoided Euler-flow reversal on a shorter length scale, i.e. separation ahead of the leading edge of the body. The presence of negative orientation or negative wall velocity is not expected to disturb the main findings of the study substantially. The paper [30] considers the implications of such reversal in a quasi-inviscid context and it would be beneficial to build on this within the present viscous-inviscid context. Parameters of special note overall in the fluid–body coupling here are the Reynolds number Re, the density ratio, the typical scaled offset width W^* of the body from the wall, the effective body thickness c_2 and orientation c_1; the broad features of their influence are described in the original theory of Sections 2, 3 and in the numerical and analytical solutions of Sections 4 and 5. Flexible bodies are also addressed briefly in Appendix B. The flexibility represents a simple model in terms of the original motivation concerning non-firm ice crystals as well as droplets and melting bodies.

Future investigations should tackle the effects of spatial three-dimensionality and time scales other than that considered in this paper. Furthermore, the original nonlinear problem of Section 2 which is very challenging merits a numerical treatment, given that it does not appear to yield rationally to an analytical treatment for $O(1)$ values of the width parameter W^* and streamwise distance X. Although we may now understand entry properties somewhat in the sense of what happens when the body is in the upper reaches of a viscous-inviscid layer close to a solid surface, the challenge is to move on to considering a body that lies in the midst of such a layer. (Here the present analysis may provide useful test cases for comparison.) The interactions then may force the body to impact on the wall. Alternatively, the body could fly away relatively far from the wall; the present study may have relevance in the latter scenario.

https://doi.org/10.1017/S0956792519000378 Published online by Cambridge University Press

Acknowledgements

Discussions with and interest from Richard Moser, Ian Roberts and Colin Hatch, all of AeroTex UK, and from Robert Bowles, Nick Ovenden, Sergei Timoshin, Samire Balta are gratefully acknowledged, as is support from EPSRC through grants EP/R511638/1, GR/T11364/01, EP/G501831/1, EP/H501665/1, EP/K032208/1 during part of this research and from UCL (IAA award) and AeroTex. The referees are thanked for their very helpful comments.

Conflicts of interest

The authors have no conflicts of interest.

References

[1] Anderson, D., Tannehill, J. C. & Pletcher, R. H. (2016) *Computational Fluid Mechanics and Heat Transfer*, Florida: CRC Press.

[2] Bhattacharyya, S., Mahapatra, S. & Smith, F. T. (2004) Influence of surface roughness on shear flow. *J. Appl. Mech.* **71**(4), 459–464.

[3] Dehghan, M. & Basirat Tabrizi, H. (2014) Effects of coupling on turbulent gas-particle boundary layer flows at borderline volume fractions using kinetic theory. *J. Heat Mass Transf. Res.* **1**(1), 1–8.

[4] Einav, S. & Lee, S. (1973) Particles migration in laminar boundary layer flow. *Int. J. Multiphase Flow* **1**(1), 73–88.

[5] Frank, M., Anderson, D., Weeks, E. R. & Morris, J. F. (2003) Particle migration in pressure-driven flow of a Brownian suspension. *J. Fluid Mech.* **493**, 363–378.

[6] Gavze, E. & Shapiro, M. (1997) Particles in a shear flow near a solid wall: effect of nonsphericity on forces and velocities. *Int. J. Multiphase Flow* **23**(1), 155–182.

[7] Gent, R., Dart, N. & Cansdale, J. (2000) Aircraft icing. *Philos. Trans. R. Soc. London. Ser. A Math. Phys. Eng. Sci.* **358**(1776), 2873–2911.

[8] Hall, G. (1964) On the mechanics of transition produced by particles passing through an initially laminar boundary layer and the estimated effect on the LFC performance of the X-21 aircraft, Technical Report, NASA.

[9] Kishore, N. & Gu, S. (2010) Wall effects on flow and drag phenomena of spheroid particles at moderate Reynolds numbers. *Ind. Eng. Chem. Res.* **49**(19), 9486–9495.

[10] Lagrée, P.-Y. (1993) Mixed convection at small Richardson number on triple deck scales. *Comptes Rendus de l'Academie des Sciences Serie II* **318**, 1167–1173.

[11] Lagrée, P.-Y. (2007) Interactive boundary layer in a Hele Shaw cell. *ZAMM-J. Appl. Math. Mech./Zeitschrift für Angewandte Mathematik und Mechanik: Appl. Math. Mech.* **87**(7), 486–498.

[12] Loisel, V., Abbas, M., Masbernat, O. & Climent, E. (2013) The effect of neutrally buoyant finite-size particles on channel flows in the laminar-turbulent transition regime. *Phys. Fluids* **25**(12), 123304.

[13] Loth, E. & Dorgan, A. J. (2009) An equation of motion for particles of finite Reynolds number and size. *Environ. Fluid Mech.* **9**(2), 187–206.

[14] Norde, E. (2017) *Eulerian Method for Ice Crystal Icing in Turbofan Engines*, University of Twente.

[15] Petrie, H., Morris, P., Bajwa, A. & Vincent, D. (1993) Transition induced by fixed and freely convecting spherical particles in laminar boundary layers, Technical report, Pennsylvania State University Park Applied Research Lab.

[16] Poesio, P., Ooms, G., Ten Cate, A. & Hunt, J. C. (2006) Interaction and collisions between particles in a linear shear flow near a wall at low Reynolds number. *J. Fluid Mech.* **555**, 113–130.

[17] Portela, L. M., Cota, P. & Oliemans, R. V. (2002) Numerical study of the near-wall behaviour of particles in turbulent pipe flows. *Powder Technol.* **125**(2–3), 149–157.

https://doi.org/10.1017/S0956792519000378 Published online by Cambridge University Press

[18] PRUESSNER, L. & SMITH, F. T. (2015) Enhanced effects from tiny flexible in-wall blips and shear flow. *J. Fluid Mech.* **772**, 16–41.
[19] PURVIS, R. & SMITH, F. T. (2016) Improving aircraft safety in icing conditions. In: P. J. Aston, A. J. Mulholland and K. Tant (editors), *UK Success Stories in Industrial Mathematics*, Springer International Publishing, New York, pp. 145–151.
[20] ROTHMAYER, A. P. & SMITH, F. T. (1998) High Reynolds number asymptotic theories. In: R. W. Johnson (editor), *The Handbook of Fluid Dynamics*, Florida: CRC Press, chapter 23–25.
[21] SCHMIDT, C. & YOUNG, T. (2009) Impact of freely suspended particles on laminar boundary layers. In: *47th AIAA Aerospace Sciences Meeting including The New Horizons Forum and Aerospace Exposition*, p. 1621.
[22] SCHMIDT, C., YOUNG, T. M. & BENARD, E. P. (2010) The effect of a particle travelling through a laminar boundary layer on transition. In: *Seventh IUTAM Symposium on Laminar-Turbulent Transition*, Springer, pp. 561–564.
[23] SMITH, F. T. (1976) Flow through constricted or dilated pipes and channels: part 2. *Q. J. Mech. Appl. Math.* **29**(3), 365–376.
[24] SMITH, F. T. (2017) Free motion of a body in a boundary layer or channel flow. *J. Fluid Mech.* **813**, 279–300.
[25] SMITH, F. T. & DANIELS, P. G. (1981) Removal of Goldstein's singularity at separation, in flow past obstacles in wall layers. *J. Fluid Mech.* **110**, 1–37.
[26] SMITH, F. T. & ELLIS, A. S. (2010) On interaction between falling bodies and the surrounding fluid. *Mathematika* **56**(1), 140–168.
[27] SMITH, F. T. & JOHNSON, E. R. (2016) Movement of a finite body in channel flow. *Proc. R. Soc. A Math. Phys. Eng. Sci.* **472**(2191), 20160164.
[28] SMITH, F. T. & JONES, M. A. (2003) AVM modelling by multi-branching tube flow: large flow rates and dual solutions. *Math. Med. Biol.* **20**(2), 183–204.
[29] SMITH, F. T., OVENDEN, N. C., FRANKE, P. T. & DOORLY, D. J. (2003) What happens to pressure when a flow enters a side branch? *J. Fluid Mech.* **479**, 231–258.
[30] SMITH, F. T. & PALMER, R. (2019) A freely moving body in a boundary layer: nonlinear separated-flow effects. *Appl. Ocean Res.* **85**, 107–118.
[31] SMITH, F. T. & SERVINI, P. (2019) Channel flow past a near-wall body. *Q. J. Mech. Appl. Math.* **72**(3), 359–385.
[32] SMITH, F. T. & TIMOSHIN, S. N. (1996) Blade-wake interactions and rotary boundary layers. *Proc. R. Soc. London Ser. A Math. Phys. Eng. Sci.* **452**(1949), 1301–1329.
[33] SMITH, F. T. & WILSON, P. L. (2013) Body-rock or lift-off in flow. *J. Fluid Mech.* **735**, 91–119.
[34] SOBEY, I. J. (2000) *Introduction to Interactive Boundary Layer Theory*, Vol. 3, Oxford Applied Engineering and Mathematics, Oxford University Press, Oxford.
[35] WANG, J. & LEVY, E. K. (2006) Particle behavior in the turbulent boundary layer of a dilute gas-particle flow past a flat plate. *Exp. Therm. Fluid Sci.* **30**(5), 473–483.
[36] YU, Z., PHAN-THIEN, N. & TANNER, R. I. (2007) Rotation of a spheroid in a Couette flow at moderate Reynolds numbers. *Phys. Rev. E* **76**(2), 026310.

A Appendix

A.1 The scalings

The reasoning below confirms that for the boundary-layer setting the main range of interest is for scaled lengths such that

$$Re^{-3/4} \ll l \ll Re^{-3/8}, \tag{A1}$$

based on estimates of the orders of magnitude present. We suppose that the typical body thickness $Re^{-1/2}\delta$ say is comparable with the thickness of the fluid-filled gap between the underbody

https://doi.org/10.1017/S0956792519000378 Published online by Cambridge University Press

and the wall and is significantly less than the boundary-layer thickness, which is of order $Re^{-1/2}$ since x_0 is of order unity. So δ is small. It is supposed further that the major flow response occurs over the same height $O(Re^{-1/2}\delta)$ by virtue of invoking a nonlinear response and the possibility of significant local alterations to the wall shear stress, for instance. The oncoming velocity profile which is linear near the wall indicates that the characteristic velocity u involved near the body is small and comparable with δ because of the dominant wall-shear effect. The typical streamwise length scale l_1 of physical importance in the sublayer flow around the body can then be estimated from balancing the order of magnitude of the inertial forces $uu_x \sim \delta^2/l_1$ against that of the prominent viscous force $Re^{-1}u_{yy} \sim Re^{-1}\delta/(Re^{-1/2}\delta)^2$, bearing in mind that y is of scale $Re^{-1/2}\delta$. The balance thus imposes l_1 as being of order δ^3. One would expect l_1, l to be comparable as the first central interactive case and so obtain a simple relationship between the fraction δ and the critical length scale with the accompanying scales

$$\delta \sim l^{1/3},\ u \sim l^{1/3},\ p \sim l^{2/3},\ y \sim l^{1/3}Re^{-1/2},\ t \gg l^{2/3} \tag{A2}$$

See [23, 20, 10, 11, 34] for related discussions of scalings. We have taken the time scale to not respond mainly to the flow inertial force. The main response is slower, yielding quasi-steady behaviour owing to fluid–body interaction. The lower limitation in (A1) corresponds to the sublayer height $|y|$ becoming comparable with the streamwise scale l and producing a quite tiny region governed by the full Navier–Stokes system. In contrast, the upper limitation in (A1) is associated with the triple deck stage where the thin sublayer around the body experiences a substantial feedback of pressure which arises from interaction with the flow outside the surrounding boundary layer. In between, where the range (A1) applies, the sublayer is controlled by thin-layer dynamics alone.

For channel flows, the corresponding range of validity of the current problem (2.3a)–(2.7b) is

$$R^{-1/2} \ll l \ll R^{1/7}. \tag{A3}$$

Here, the representative length L^* is the channel width a^*, such that the dimensional length of the body is a^*l, and likewise R is the Reynolds number U^*a^*/ν^* based on a^*. See [23, 24].

B Appendix

B.1 If the body is flexible

The model we use for the influence of an elastic upper surface of the body has the form

$$e_2\frac{\partial^2 g^+}{\partial X^2} = P_1^* - \pi_0 \tag{B1}$$

where the positive constant e_2 is a scaled longitudinal tension of the overbody surface and the constant π_0 is the scaled base pressure within the body relative to the incident pressure. Here, the boundary conditions on the unknown shape function g^+ are, without loss of generality,

$$g^+ = 0 \text{ at } X = 0, 1. \tag{B2}$$

The physical sense of the relation (B1) combined with (B2) can be seen in the property that a positive pressure difference $P_1^* - \pi_0$ promotes a positive curvature and hence an overall decrease

https://doi.org/10.1017/S0956792519000378 Published online by Cambridge University Press

in the overbody shape, as we might expect. The equations (B1) and (B2) are coupled with the body-motion equations

$$Mh_{TT} = -\int_0^1 P_1^* dX, \tag{B3}$$

$$I\theta_{TT} = -\int_0^1 (X-\beta)P_1^* dX, \tag{B4}$$

from (2.3a) and (2.3b) but bearing in mind the comparatively high-pressure magnitudes P_1^* acting on top of the body, and with (3.12) requiring

$$P_1^*(X,T) = \lambda^2 Y_0^*(f^+(1,T) - f^+(X,T)), \tag{B5}$$

subject now to

$$f^+(X,T) = g^+(X,T) + h(T) + (X-\beta)\theta(T). \tag{B6}$$

The system of interest is thus (B1)–(B6) where in particular $h(T), \theta(T)$ are to be found. Combining (B1), (B5) and (B6) leads in effect to a spatial problem for f^+, namely to solve

$$e_2 \frac{\partial^2 f^+}{\partial X^2} = \lambda^2 Y_0^*(f^+(1,T) - f^+(X,T)) - \pi_0, \tag{B7}$$

subject to $f^+ = h - \beta\theta$ at $X = 0$ and $f^+ = h + (1-\beta)\theta$ at $X = 1$ in view of (B2). Hence, the shape solution is

$$f^+ = A\sin\alpha X + B\cos\alpha X + C \tag{B8}$$

where the constants are given by $A = \{\theta\cos\alpha + \frac{(1-\cos\alpha)\pi_0}{\lambda^2 Y_0^*}\}\frac{1}{\sin\alpha}$, $B = -\theta + \frac{\pi_0}{\lambda^2 Y_0^*}$, $C = h + (1-\beta)\theta - \frac{\pi_0}{\lambda^2 Y_0^*}$ and the effective wavenumber $\alpha = ((\lambda^2 Y_0^*)e_2)^{1/2}$. The pressure solution then follows from (B5), following which substitution into (B3) and (B4) yields evolution equations for $h(T), \theta(T)$.

The latter equation is found to take the form, after a constant is added to the θ value,

$$\frac{I\theta_{TT}}{\lambda^2 Y_0^*} = -D\theta, \tag{B9}$$

with

$$D = \frac{1-\beta+\beta\cos\alpha}{\alpha\sin\alpha} - \frac{1}{\alpha^2}. \tag{B10}$$

The evolution of θ therefore depends on the constant coefficient D. A plot of D as α, β vary is presented in Figure B.1. There is seen to be a wide range of values of the wavenumber α for which D is positive, corresponding to relative stability as the scaled angle θ then oscillates in time, and also a wide range where D is negative, meaning that instability occurs since θ grows exponentially in time. The associated $h(T)$ grows algebraically in time in the quasi-stable case in general but exponentially in the unstable case. The location β also plays a role in determining the

https://doi.org/10.1017/S0956792519000378 Published online by Cambridge University Press

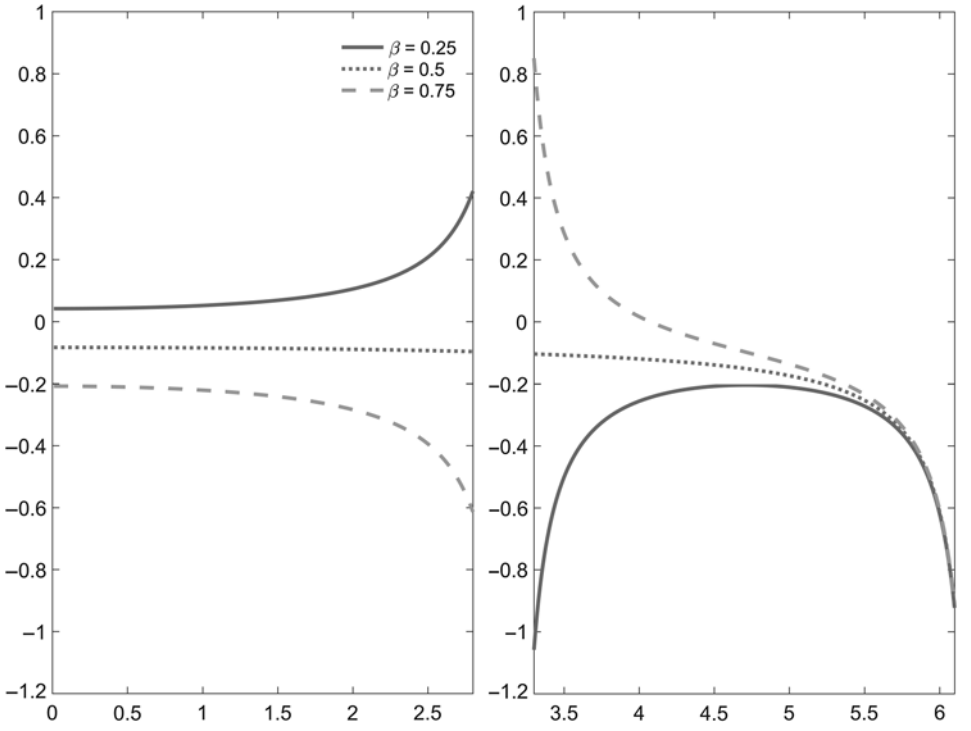


FIGURE B.1. Plots of D against α for a body with flexible shape with $\beta = 0.25, 0.5$ and 0.75.

sign of D as illustrated in Figure B.1. α is well-defined away from any positive multiple of π with D notably becoming increasingly independent of β as α approaches values of $2n\pi$, $n = 1, 2, 3, ...$

https://doi.org/10.1017/S0956792519000378 Published online by Cambridge University Press